Available online at www.sciencedirect.com
SCIENCE DIRECT
Ultrasonics 44 (2006) 64–72
Ultrasonics
www.elsevier.com/locate/ultras

Vibration of piezoelectric elements surrounded by fluid media

Hemant Kamath, Morten Willatzen *, Roderick V.N. Melnik

University of Southern Denmark, Mads Clausen Institute, Grundtvigs Alle 150, Sonderborg DK-6400, Denmark

Received 19 May 2005; accepted 3 August 2005
Available online 19 September 2005

Abstract

In this paper we analyse vibrational characteristics of piezoceramic shells surrounded by acoustic media. Main results are presented for radially polarized piezoceramic PZT5 elements of hollow cylindrical shapes. The coupling in the radial direction between the solid and the acoustic media is accounted for indirectly, via impedance boundary conditions. The model based on such impedance boundary condition approximations offers a robust simplified alternative to a full scale fluid–solid interaction modelling. By using this model, we analyse numerically the influence of the boundary conditions imposed in the axial direction for long, medium, and short (disk-like) piezoceramic elements.

PACS: 43.40.Rj; 43.38.Fx

Keywords: Piezoelectrics; Impedance; Fluid–solid coupling; Finite-element analysis

1. Introduction

Piezoceramic elements constitute an important part of smart materials and structures technology with applications ranging from medical imaging and aerospace to nondestructive testing, ultrasonic flow-metering and ocean engineering. Such elements come in different forms and shapes and can be prefabricated by using different polarization directions. Hollow cylindrical shells are among most frequently used elements in many areas, including ultrasonics applications [2,18,12,6,13]. While vibrational patterns of purely elastic waves in such structures have been analysed for many decades, the analysis of coupled electroelastic wave propagation is of more recent origin.

Many previous results have been obtained in the context of guided elastic wave analysis using circumferential and longitudinal modes, but the situation becomes more complicated if the cylinder is made of some anisotropic material, such as piezoelectric ceramics. These polycrystallic solids have dipoles in each crystal which are stochastically oriented in general, but tend to be parallel in small domains. Preliminary polarization of the piezoceramics orders these domain in one single direction. The fact, often overlooked in the literature, is that only in the case where the external field has some symmetry properties, it is possible to simplify constitutive relations in such a way that they can be written with constant coefficients in some appropriate curvilinear system of coordinates. In this paper we consider the case of radial preliminary polarization which results in a strong coupling between elastic and electric fields [3,11]. We are interested in a situation where the structure is in contact with another acoustically active media, e.g., a fluid and/or gas. In order to analyse such problems at a full scale, one needs to consider also the coupling between solid and fluid/gas media. If the solid is made of an active material (the situation considered in this paper), then the model for such a full scale modelling becomes quite complicated [14,4,11]. Numerical methodologies for the solution of such fully coupled problems are quite involved and are at the beginning of their development.

* Corresponding author. Tel.: +45 6550 1682; fax: +45 6550 1660.
E-mail address: Willatzen@mci.sdu.dk (M. Willatzen).

0041-624X/$ - see front matter © 2005 Elsevier B.V. All rights reserved.
doi:10.1016/j.ultras.2005.08.003

In this paper we propose a different path. As our main interest is in vibrational characteristics of the solid element, we account for the surrounding acoustic media indirectly, via impedance boundary conditions. In this case we can analyse electromechanical waves in hollow cylinders by using *only* the equation of motion and the Maxwell equation accounting for conservation of electric charge. For the case of radially polarized cylinders, these equations are strongly coupled by constitutive relations between stresses, strains, and the electric field. In all results reported here we use the crystal symmetry group C_{6v} (6 mm) so that axisymmetrical conditions can be applied. We organize the rest of the paper as follows. In Section 2 we provide the details of the model that describes vibrations of axisymmetric cylindrical shells preliminary polarized in the radial direction. Section 3 gives geometric details of piezoceramic elements we analyse, as well as the information on their physical characteristics. The procedure describing coupling between the solid piezoceramic element and the surrounding acoustic media is discussed in Section 4. In this section we also formulate the impedance boundary conditions used in our calculations. Section 5 reports the results of numerical experiments carried out for different boundary conditions and different geometric characteristics of the elements under consideration.

2. Model of dynamic piezoelectricity for axisymmetric cylindrical shells

The model describing vibrations of piezoelectric axisymmetric cylindrical shells can be written as follows (e.g., [7,11]):

$$\rho\frac{\partial^2 u_1}{\partial t^2}=\frac{\partial}{\partial r}(\sigma_{rr})+\frac{\partial}{\partial z}(\sigma_{rz})+\frac{\sigma_r-\sigma_\theta}{r}+f_1, \tag{2.1}$$

$$\rho\frac{\partial^2 u_2}{\partial t^2}=\frac{\partial}{\partial r}(\sigma_{rz})+\frac{\partial}{\partial z}(\sigma_z)+\frac{1}{r}(\sigma_{rz})+f_2, \tag{2.2}$$

$$\frac{1}{r}\frac{\partial}{\partial r}(rD_r)+\frac{\partial D_z}{\partial z}=0, \tag{2.3}$$

where $\mathbf{u}=(u_1,u_2)$ is the displacement (in r and z directions, respectively), ρ is the density of the piezoceramics, σ_{ij} are stress components, $\mathbf{F}=(f_1,f_2)$ is the piezoelectric body forces, and $\mathbf{D}=(D_r,D_z)$ is the electric displacement (induction) vector.

The type of preliminary polarization determines the form of constitutive equations which for the case of radial preliminary polarization yield [3,11]

$$\begin{aligned}
&\sigma_{rr}=c_{33}\epsilon_r+c_{13}(\epsilon_\theta+\epsilon_z)-e_{33}E_r,\\
&\sigma_{\theta\theta}=c_{13}\epsilon_r+c_{11}\epsilon_\theta+c_{12}\epsilon_z-e_{13}E_r,\\
&\sigma_{zz}=c_{13}\epsilon_r+c_{12}\epsilon_\theta+c_{11}\epsilon_z-e_{13}E_r,\quad \sigma_{rz}=2c_{44}\epsilon_{rz}-e_{15}E_z,\\
&D_r=e_{33}\epsilon_r+e_{13}(\epsilon_\theta+\epsilon_z)+\varepsilon_{33}E_r,\quad D_z=2e_{15}\epsilon_{rz}+\varepsilon_{11}E_z,
\end{aligned} \tag{2.4}$$

where the electric field $\mathbf{E}=(E_r,E_z)$ is defined by its electrostatic potential ψ ($E_r=-\partial\psi/\partial r$, $E_z=-\partial\psi/\partial z$), c_{ij} are elastic coefficients, e_{kl} are piezomoduli, ε_{ii} are dielectric permittivity, and ϵ_{ij} are strain components. The relationships between the components of strain and displacements are defined in the Cauchy form:

$$\epsilon_r=\frac{\partial u_1}{\partial r},\quad \epsilon_\theta=\frac{u_1}{r},\quad \epsilon_z=\frac{\partial u_2}{\partial z},\quad 2\epsilon_{rz}=\frac{\partial u_1}{\partial z}+\frac{\partial u_2}{\partial r}. \tag{2.5}$$

The system (2.1)–(2.5) is supplemented by corresponding boundary and initial conditions.

3. Geometric and physical characteristics of the structure

The model (2.1)–(2.5) is applied in the subsequent sections to the numerical analysis of vibration patterns of hollow cylindrical shells. In particular, we focus on the analysis of cylinders with different ratio between the thickness and the lateral length of cylinder. This analysis is performed for the model (2.1)–(2.5) with impedance boundary condition approximations which we develop in Section 4. In this section we provide details of geometric and physical characteristics of the structure.

The structure under consideration is depicted in Fig. 1. By varying the ratio between L_z and $L_r=R_1-R_0$ (see Fig. 1), we consider three typical situations encountered in practical applications. In particular, the thickness of the cylinder, L_r, is kept the same for all experiments reported in Section 5 (1 mm), while the length of the cylinder in the axial direction is varied. Namely, we have

- $L_z=L_r/40$ (Case (i)—short structure),
- $L_z=L_r$ (Case (ii)—medium structure), and
- $L_z=10L_r$ (Case (iii)—long structure).

The analysis is carried out for clamped ends lateral boundary conditions as well as for the relaxed conditions which accounted frequently in applications of piezoceramic elements (e.g., [8,4,15]). We analyse piezoceramic elements made of PZT5 (e.g., [16,11]). These elements are surrounded by acoustic media from inside and outside (water and air, respectively). The computational domain is symmetric with respect to the r-axis, and hence Neumann's boundary conditions are imposed at that axis. The physical characteristics of the structure are provided in Table 1.

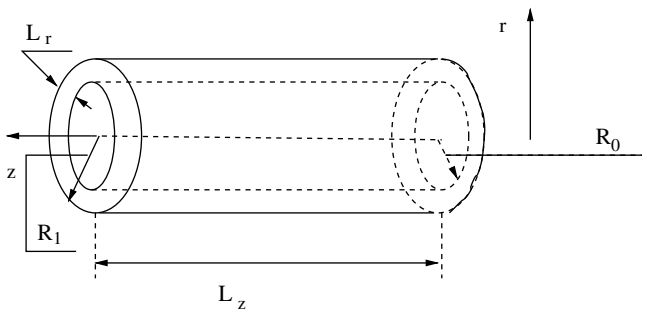

Fig. 1. Geometry of the structure under consideration.

Table 1
Piezoelectric and acoustic characteristics of the analysed structure

$c_{11} = 1.21 \times 10^{11}$ N/m^2	$c_{12} = 7.54 \times 10^{10}$ N/m^2	$c_{13} = 7.52 \times 10^{10}$ N/m^2
$c_{33} = 1.11 \times 10^{11}$ N/m^2	$c_{44} = 2.11^{10}$ N/m^2	$e_{33} = 15.8$ C/m^2
$e_{15} = 12.3$ C/m^2	$e_{13} = -5.4$ C/m^2	$\varepsilon_{11} = 1.53 \times 10^{-8}$ F/m^2
$\varepsilon_{33} = 1.51 \times 10^{-8}$ F/m^2	$c_0 = 1509.37$ m/s	$c_1 = 343.7$ m/s

Our next step is to consider a simple and robust model for coupling of the piezoceramic shell to the surrounding acoustic media. This is achieved with impedance boundary conditions, as explained in the next section.

4. Coupling to the acoustic media and boundary conditions

The basic model for coupling between an active solid material, such as the piezoceramic element under consideration, and surrounding acoustic media can be derived via the concept of acoustic pressure [9]. As the acoustic pressure is coupled to the flow velocity, the model (2.1)–(2.5), given for axisymmetric waves, should be supplemented by two pairs of three equations. Namely, in each such a pair we have to deal with the continuity equation coupled to two equations resulting from Euler's vector equation with respect to components of the fluid particle velocity $\mathbf{v}^{(i)} = (v_r^{(i)}, v_z^{(i)})$, $i = 0, 1$ on each side of the hollow piezoceramic shell. If we denote by ρ_i, c_i, and p_i, $i = 0, 1$ densities, speeds of sound, and acoustic pressures in the internal and external acoustic media, we have six partial differential equations to supplement model (2.1)–(2.5):

$$\frac{1}{\rho_i c_i^2}\frac{\partial p_i}{\partial t} + \frac{1}{r}\frac{\partial\left(r v_r^{(i)}\right)}{\partial r} + \frac{\partial v_z^{(i)}}{\partial z} = 0, \quad \rho_i \frac{\partial v_r^{(i)}}{\partial t} + \frac{\partial p_i}{\partial r} = 0,$$
$$\rho_i \frac{\partial v_z^{(i)}}{\partial t} + \frac{\partial p_i}{\partial z} = 0. \tag{4.1}$$

We further note that (4.1) are coupled to (2.1)–(2.5) via the condition for continuity of radial stresses at the fluid–solid interface:

$$\sigma_{rr}(R_0, z, t) = P_0(R_0, z, t),$$
$$\sigma_{rr}(R_1, z, t) = -P_1(R_1, z, t), \tag{4.2}$$

where the acoustic pressures of the flows on the internal and external surfaces are denoted $P_0(R_0, z, t)$ and $P_1(R_1, z, t)$, respectively. In the general case, the conditions coupling (4.1) and (2.1)–(2.5) are dynamic and are difficult to treat numerically. Results on such a treatment are known only for some special cases (e.g., [11]). Here, we propose a different path to the solution of this problem. First, we limit ourselves to the harmonic approximation by assuming the solution in the form:

$$u_k = \tilde{u_k}\exp(-\mathrm{i}\omega t), \quad k = 1, 2, \quad \psi = \tilde{\psi}\exp(-\mathrm{i}\omega t), \tag{4.3}$$

where i is the imaginary unit, $\omega = 2\pi f$, and f is the frequency (all values reported in Section 5 are given in terms of f). In this case the model (2.1)–(2.5) can be simplified by moving from the time to frequency domain. As we move from the time to frequency domain in the problem formulation, we omit the tilde in the equations that follows. We consider the situation where the cylinder is excited by an electric pulse with pre-defined applied potential difference $V(t)$

$$\psi = V/2, \quad r = R_0; \quad \psi = -V/2, \quad r = R_1. \tag{4.4}$$

In addition, we have to impose the electric boundary conditions at the lateral ends of the cylinder $z = z_1$ and $z = z_2$:

$$D_z(r, z_j) = 0, \quad j = 1, 2. \tag{4.5}$$

Next, we simplify the model by replacing the electromechanical coupling with mechanical boundary conditions that express continuity of radial stresses and velocity via the impedance boundary conditions [9]. Such conditions have important applications in acoustics and have recently been analysed in the context of time-reversal techniques important for improved refocusing in such applications as medicine, communications, nondestructive testing, and underwater acoustics [1]. Impedance boundary conditions are used also frequently in the context of the acoustic sensitivity analysis and design optimization (e.g., [17]). The acoustic impedance corresponding to water/air as the surrounding fluid is defined here as follows (e.g., [9, Chapter 5]):

$$Z_{\mathrm{wa}} = \mathrm{i}\rho_0 c_0 H_0^2(\omega R_0/c_0)/H_1^2(\omega R_0/c_0),$$
$$Z_{\mathrm{air}} = \mathrm{i}\rho_1 c_1 H_0^2(\omega R_1/c_1)/H_1^2(\omega R_1/c_1), \tag{4.6}$$

where, as before, c_i and ρ_i, $i = 1, 2$ are the speeds of sound in and densities of water and air, respectively, and H_i^2, $i = 0, 1$ are Hankel functions of the second kind of zeroth and first orders, respectively. Our application of impedance boundary conditions (4.6) assumes continuity of radial component of velocity at the fluid–solid interface, while conditions (4.2) imply continuity of radial stress in the solid and pressure in the inviscid fluid:

$$\sigma_{rr}(R_0, z, t) = \mathrm{i}\omega Z_{\mathrm{wa}} u_1(R_0, z, t);$$
$$\sigma_{rr}(R_1, z, t) = -\mathrm{i}\omega Z_{\mathrm{air}} u_1(R_1, z, t). \tag{4.7}$$

The (rz)-component of stress in all our experiments reported in Section 5 is taken to be zero:

$$\sigma_{rz}(R_0, z, t) = 0; \quad \sigma_{rz}(R_1, z, t) = 0, \tag{4.8}$$

since we have inviscid fluid on the inside and outside. At the same time, the mechanical boundary conditions at the axial/lateral ends of the cylinder will vary and we will analyse the dependence of the solution on this variation. In particular, first we will be interested in the clamped boundary conditions. These conditions are frequently used in applications, although it is known that they are quite difficult to satisfy in practice (e.g., [15]). Hence, we relax these conditions by considering a series of computational experiments with transversely free structures as well as transversely and longitudinally free structures. From a series of computational experiments reported in the next section we determine typical critical frequencies for the structures under consideration, and provide details of the analysis of vibration patterns for one such frequency.

5. Numerical results and discussion

The model discussed in the previous sections has been solved numerically. The set of partial differential equations (2.1)–(2.5) and the associated boundary conditions (4.7) and (4.8) for fluid coupling were implemented in Matlab-based Femlab [5] using the finite-element methodology [19]. The problem was solved in cylindrical coordinates and—given the independence of the problem of the azimuthal coordinate—the computational domain simplifies to a two-dimensional rectangular region in z and r. Computations were carried out on a sequence of grids with triangular elements increasing in numbers from 264 to 1700 to ensure that grid independence of dependent variables was achieved for all cases presented here.

In what follows we discuss the results of computational experiments performed for three structures, short, medium, and large. Three representative examples were chosen to represent such structures as described in Section 3. As we have mentioned, we will consider three main types of the boundary conditions for the ends of the cylinder ($z = z_1$ and $z = z_2$), namely:

- $u_1 = 0$; $u_2 = 0$ [Case (a)],
- $u_2 = 0$; $\sigma_{rz} = 0$ [Case (b)], and
- $\sigma_{rr} = 0$; $\sigma_{rz} = 0$ [Case (c)].

These three boundary-condition cases reflect typical support conditions in the sense that Case (a), Case (b), and Case (c) correspond to a longitudinally and transversely clamped structure, a longitudinally clamped but transversely free structure, and a longitudinally and transversely free structure, respectively.

Consider the medium cylinder first. In Fig. 2, a frequency sweep of the maximum absolute radial displacement u_1 as calculated over the whole piezoceramic structure is shown for the medium structure with $L_z = L_r = 10^{-3}$ m and boundary conditions (b). In a series of computational experiments we have performed, these boundary conditions lead to a practical independency of the results along the z-direction. The model reproduces the results of the one-dimensional case where the impedance boundary conditions are well justified because the reflected and transmitted waves can be determined in terms of the impedance as a function of the geometry, the velocity of sound and the density of the medium (e.g., [10]).

It is evident from our Fig. 2 that two resonant peaks at 1.885 MHz and 1.95 MHz exist, the former being slightly larger corresponding to $\max|u_1| = 90$ Å. In the following, we present results exclusively at 1.885 MHz for three cases of boundary conditions at the lateral boundary ends, as outlined above. Furthermore, we present results for all boundary-condition cases for the three structures, medium, short, and long, as we described in Section 3. In all these cases the impedance boundary conditions, as outlined by (4.6)–(4.8), are imposed. We note that for the long structure with boundary conditions corresponding to Cases (a) and (c), resonance frequencies are found to be at

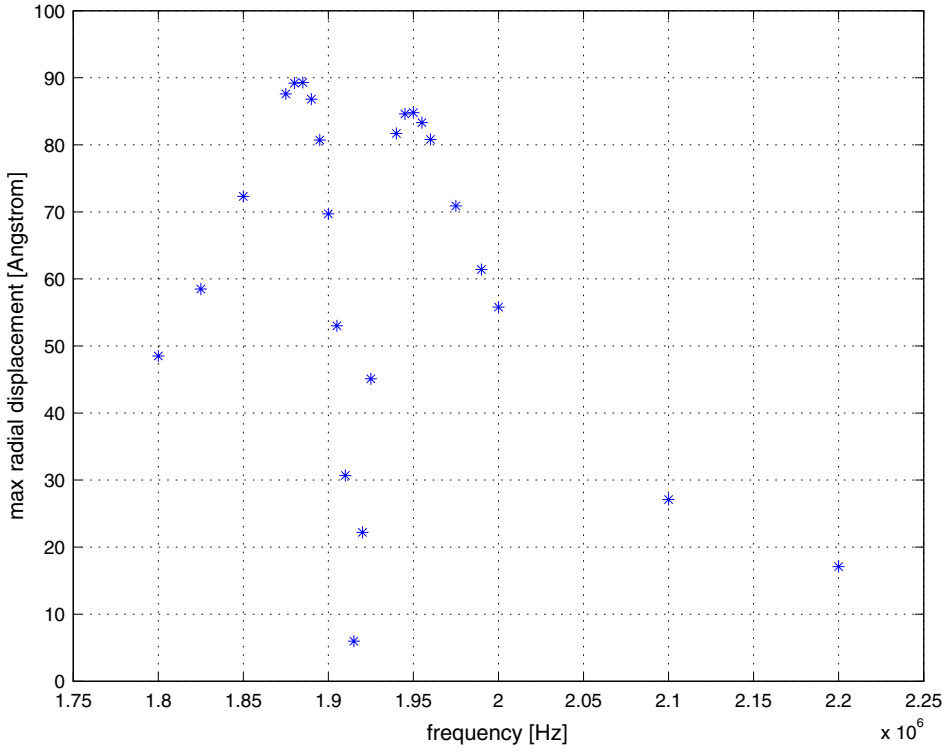

Fig. 2. Frequency sweep of the maximum absolute radial displacement $\max|u_1|$ for the full medium structure with boundary condition (b).

1.92 MHz and 1.98 MHz, respectively. In case with boundary conditions (c), two resonance peaks are observed at 1.89 MHz and 1.98 MHz, the latter being approximately 10% larger in maximum radial displacement as compared to the former. At this point, it is important to mention that qualitative differences in the spatial dependency of displacements with frequency near the resonance are not observed. Hence, it is reasonable to compare—as mentioned above—spatial displacement curves at one given frequency for all three types of boundary conditions. Indeed, our numerical experiments confirm that the qualitative spatial displacement dependencies for the short and medium structures also are unchanged at frequencies close to resonance.

In Fig. 3 (upper), u_1 for the medium structure is plotted versus z along the inner boundary facing water in Case (a) with longitudinally and transversely clamped support conditions. The displacement u_1 reaches its maximum value of approximately 90 Å at the center of the structure and decreases to 0 at the end points $z = 0$ and $z = L_z = 1$ mm as it must. Results for u_1 in Case (b) show that $u_1 \approx 89$ Å and constant as a function of z (Fig. 3 (middle)) while u_1 in Case (c) varies symmetrically around the center z value with a double-peak structure having maximum and minimum absolute values of 6.17 Å and 5.88 Å (Fig. 3 (lower)). The computed results reveal that the average $1/L_z \int_{z=0}^{z=L_z} u_1 \, dz$ is largest in Case (b) and that u_1 is almost uniform over z. Hence, for most device applications where a large and uniform displacement is sought it is beneficial to support the piezoceramic structure rigidly against longitudinal motion while allowing free motion of shear displacements at the top- and bottom-boundary ends. Note, that all displacement results are symmetric around the center z value: $z = L_z/2$ due to the symmetry of the mathematical problem at hand.

Consider next the long structure with $L_r = 10^{-3}$ m and $L_z = 10^{-2}$ m. In Fig. 4 (upper), u_1 is plotted versus z at the inner boundary side facing water corresponding to Case (a) boundary conditions. Evidently, u_1 varies periodically with approximately the same distance between peaks and valleys as observed in Fig. 3 (upper) for the medium structure (in the latter case assigning the top- and bottom-ends as valleys). The radial displacement u_1 peaks near the center $z = L_z/2$ at a value of approximately 90 Å and decays to 0 at the top- and bottom-boundary ends. In Fig. 4 (middle), u_1 is plotted against z at the inner boundary side corresponding to Case (b) boundary conditions (long structure). Similar to what is found in the medium structure with Case (b) boundary conditions, u_1 is large (approximately 89 Å) and almost uniform. Fig. 4 (lower) shows u_1 for Case (c) boundary conditions as a function of z at the inner boundary side. The spatial vibration pattern is complicated and nonuniform although large peak values of u_1 equal to approximately 130 Å are found, however, all displacement results are symmetric around the center z value: $z = L_z/2$ for the same reason as given above.

Results for the short structure with $L_z = 1/(40L_r) = 2.5 \times 10^{-5}$ m are shown in Fig. 5 (upper). The maximum

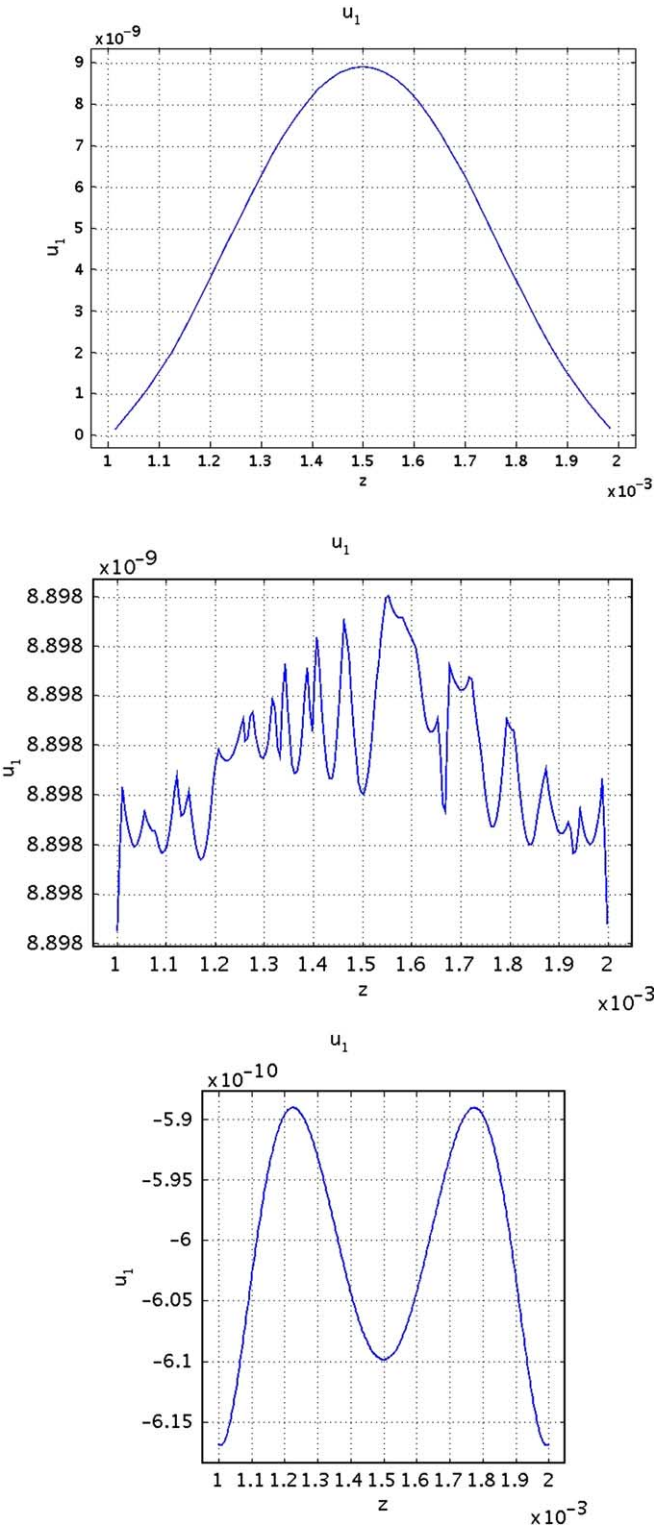

Fig. 3. Plots of the radial displacement value u_1 along the inner boundary side facing water (medium structure). The upper, middle, and lower plots correspond to Case (a), Case (b), and Case (c) boundary conditions, respectively. The first (second) axis is z (u_1) measured in m.

radial displacement is considerably smaller ($u_1 \approx 0.25$ Å) than in the long- and medium-structures cases with Case (a) boundary conditions. The reason is that the longitudi-

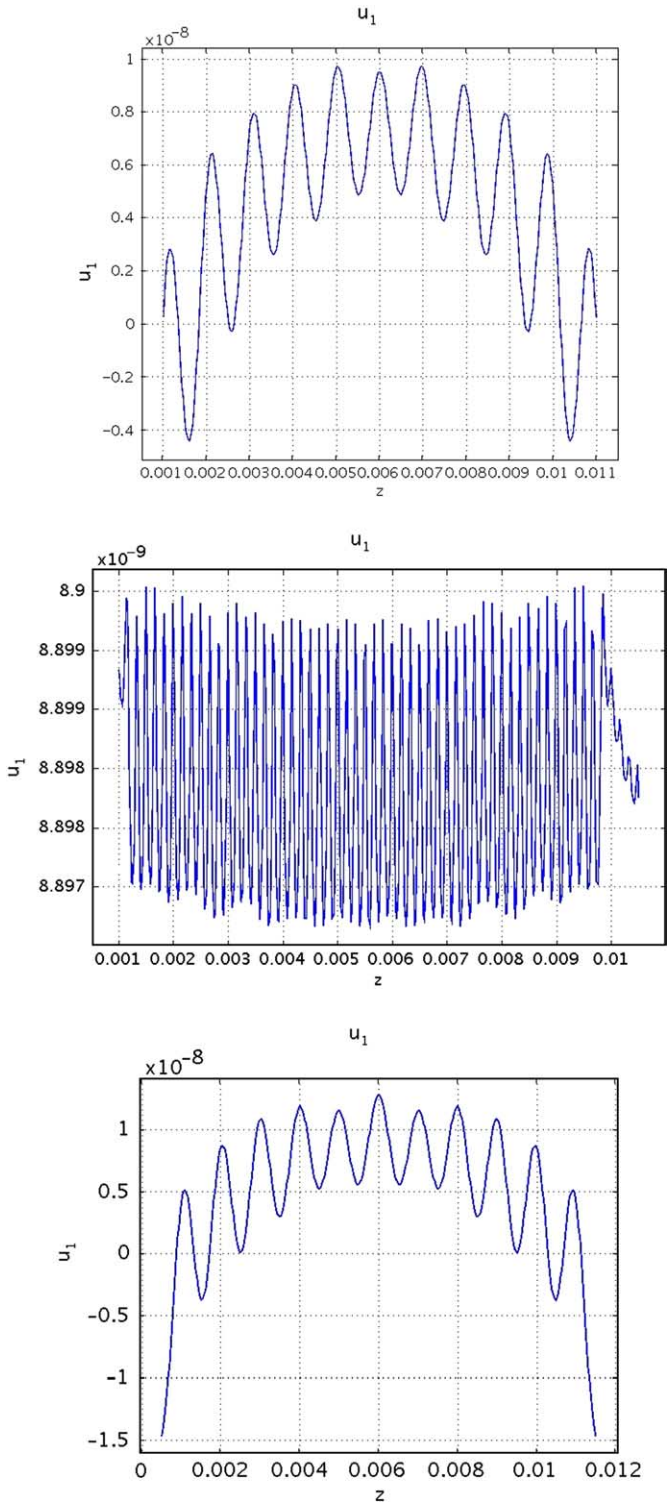

Fig. 4. Plots of the radial displacement value u_1 along the inner boundary side facing water (long structure). The upper, middle, and lower plots correspond to Case (a), Case (b), and Case (c) boundary conditions, respectively. The first (second) axis is z (u_1) measured in m.

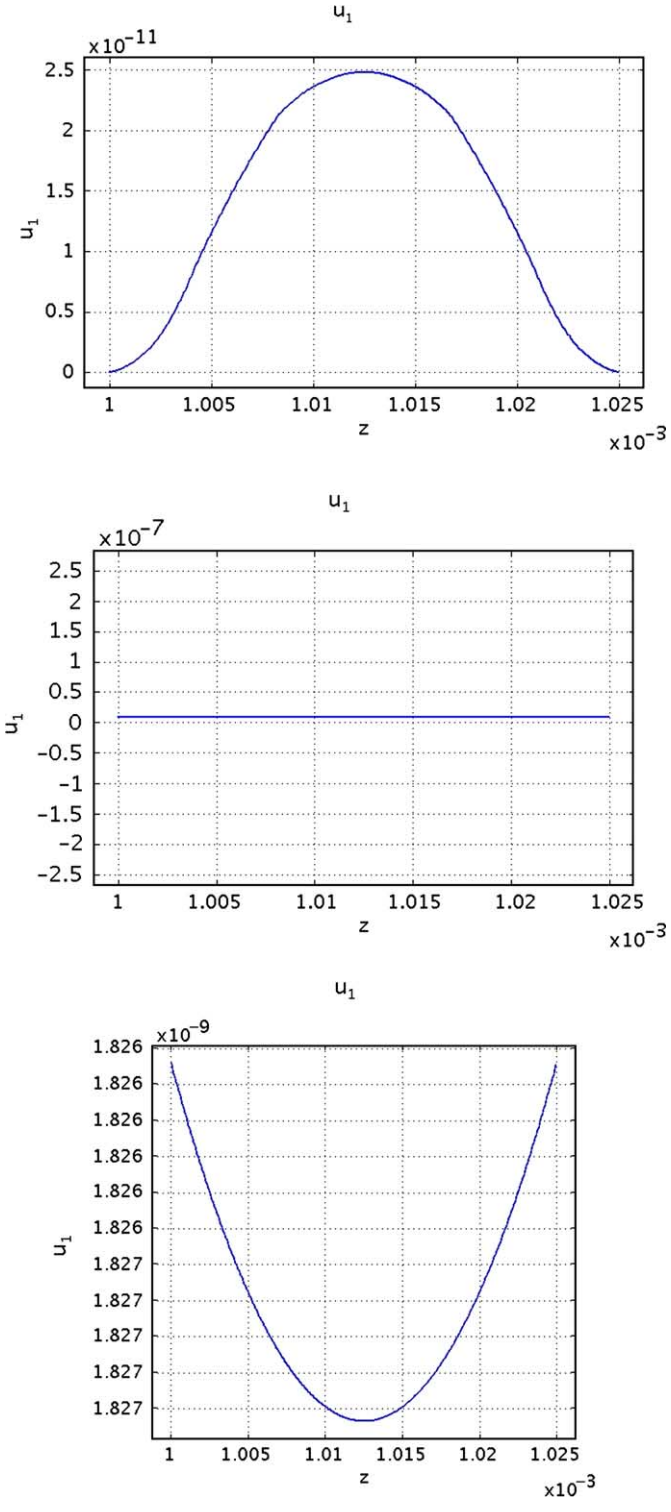

Fig. 5. Plots of the radial displacement value u_1 along the inner boundary side facing water (short structure). The upper, middle, and lower plots correspond to Case (a), Case (b), and Case (c) boundary conditions, respectively. The first (second) axis is z (u_1) measured in m.

nal and transverse vibrational wavelengths are much larger than L_z. Hence, wave motion is almost prohibited in the case with completely clamped boundaries: $u_1 = u_2 = 0$. In Fig. 5 (middle), u_1 is shown as a function of z at the inner boundary side corresponding to Case (b) boundary conditions. Results are indeed quite similar to those obtained with Case (b) boundary conditions in the medium- and long-structure cases, i.e., u_1 is large (approximately 89 Å)

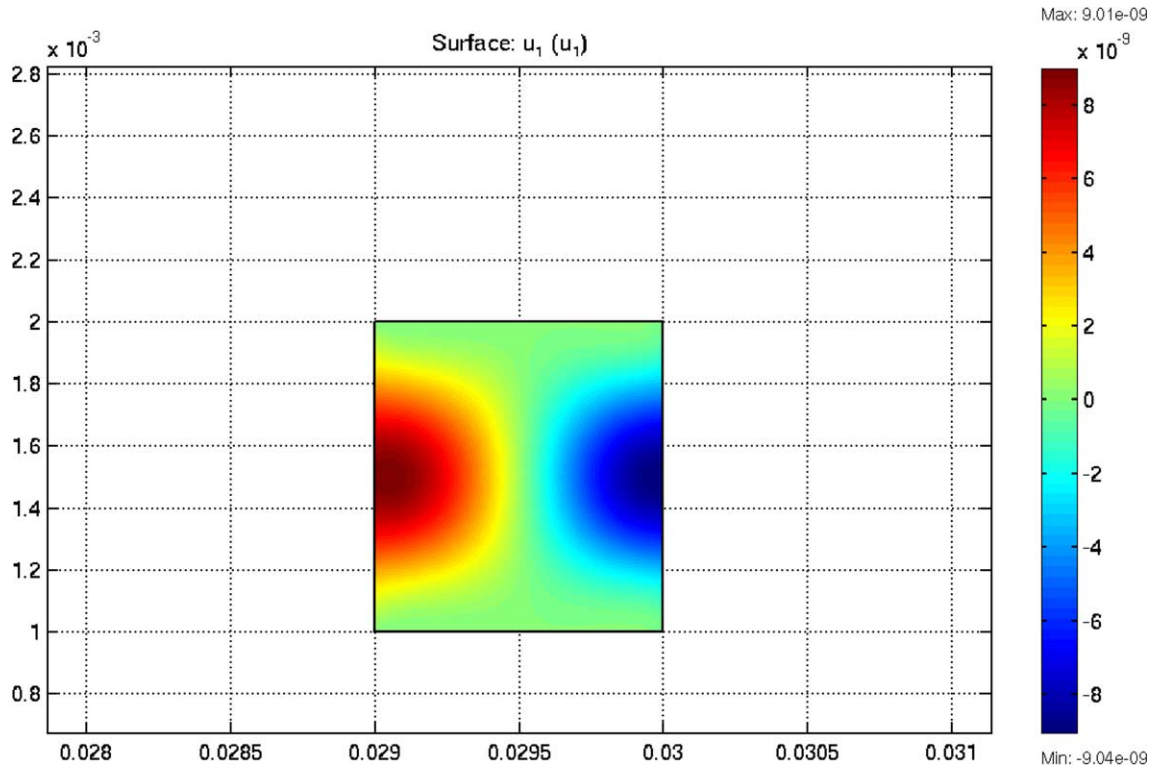

Fig. 6. Contour plot of the radial displacement value u_1 for the full medium structure with Case (a) boundary conditions. The first (second) axis is r (z) measured in m; the color bar values of u_1 are in m. (For interpretation of the references in color in this figure legend, the reader is referred to the web version of this article.)

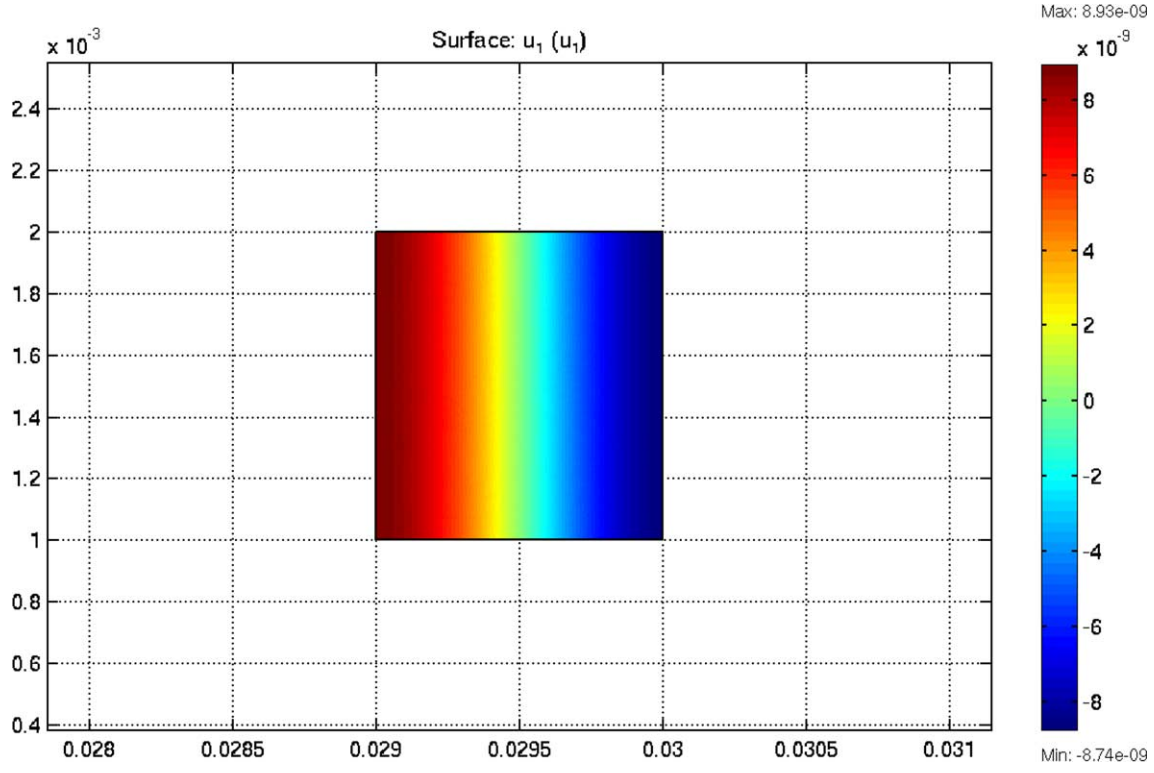

Fig. 7. Contour plot of the radial displacement value u_1 for the full medium structure with Case (b) boundary conditions. The first (second) axis is r (z) measured in m; the color bar values of u_1 are in m. (For interpretation of the references in color in this figure legend, the reader is referred to the web version of this article.)

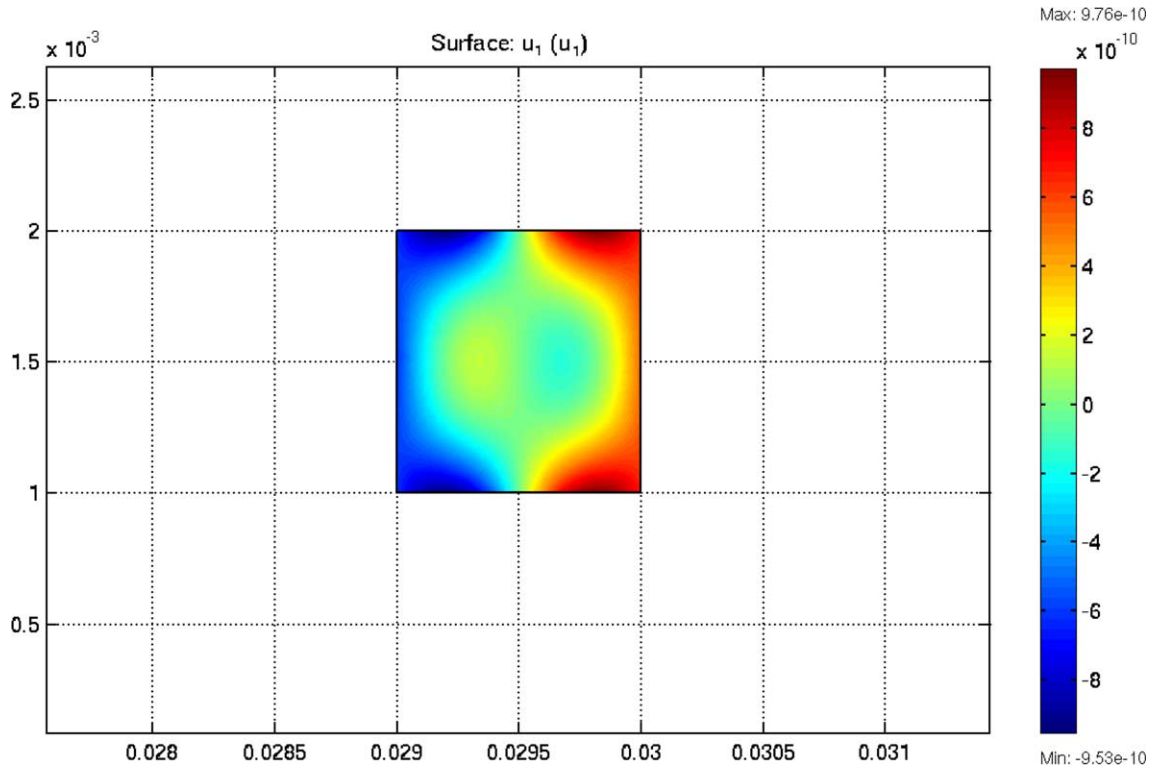

Fig. 8. Contour plot of the radial displacement value u_1 for the full medium structure with Case (c) boundary conditions. The first (second) axis is r (z) measured in m; the color bar values of u_1 are in m. (For interpretation of the references in color in this figure legend, the reader is referred to the web version of this article.)

and almost uniform. In Fig. 5 (lower), u_1 results are shown corresponding to Case (c) boundary conditions. Evidently, u_1 is almost uniform but smaller in average as compared to results obtained for Case (c) boundary conditions in the long- and medium-structure cases. Again, all displacement results are symmetric around the center z value: $z = L_z/2$ given the symmetry of the problem.

In Fig. 6, a contour plot of u_1 for the entire medium structure ($2.9\times10^{-2}\,\text{m} \leqslant r \leqslant 3\times10^{-2}\,\text{m},\ 0 \leqslant z \leqslant 10^{-3}\,\text{m}$) is shown with Case (a) boundary conditions. The displacement shows symmetry around the center value of z ($=L_z/2$) as it must given the symmetry of the system of differential equations and the boundary conditions. As mentioned earlier (Fig. 3 (upper)), the maximum radial displacement value occurs at the center z value at the inner- and outer-boundary sides. Note, that no symmetry exists with respect to the center r value ($r = L_r/2 = 2.95\times10^{-2}\,\text{m}$) due to the cylindrical nature of the problem.

In Fig. 7, a contour plot of u_1 is shown for the entire medium structure with Case (b) boundary conditions. Clearly, u_1 varies over the top- and bottom-boundary ends, however, u_1 is constant with respect to variations in z. In actual fact, it can easily be shown that a solution set exists of the form:

$$u_1(r,z) \equiv u_r, \quad u_2(r,z) = 0, \quad \psi(r,z) = ar, \tag{5.1}$$

where a is a constant, fulfilling (trivially the boundary condition: $u_2 = 0$) and the boundary condition:

$$\sigma_{rz} = c_{44}\left(\frac{\partial u_1}{\partial z} + \frac{\partial u_2}{\partial r}\right) - \varepsilon_{11}\frac{\partial \psi}{\partial z} = 0, \tag{5.2}$$

everywhere at the top- and bottom-boundary ends. The general symmetry of the problem mentioned above is again reflected in the results.

Finally, in Fig. 8, u_1 is shown versus z and r for the full geometry corresponding to Case (c) boundary conditions. Results are symmetric with respect to a reflection in the $z = L_z$ line due to the symmetry of the problem but peak u_1 values of approximately 10 Å are now found at locations $r \approx 2.92\times10^{-2}\,\text{m}$ and $r \approx 2.98\times10^{-2}\,\text{m}$ at the top- and bottom-boundary ends.

References

[1] C. Bardos, M. Fink, Mathematical foundations of the time reversal mirror, Asymptot. Anal. 29 (2) (2002) 157–182.
[2] G.R. Buchanan, C.B.Y. Yii, Effect of symmetrical boundary conditions on the vibration of thick hollow cylinders, Appl. Acoust. 63 (2002) 547–566.
[3] W.-Q. Chen, Problems of radially polarised piezoelectric bodies, Int. J. Solids Struct. 36 (1999) 4317–4332.
[4] P.-C. Eccard, H. Landes, R. Lerch, Applications of finite element simulations to acoustic wave propagation within flowing media, Int. J. Comput. Appl. Technol. 11 (1998) 163–169.
[5] Femlab 3.0 Reference Manual, Comsol Inc., Burlington, Massachusetts, USA.
[6] P.F. Hou, H.M. Wang, H.J. Ding, Analytical solution for the axisymmetric plane strain electroelastic dynamics of a special

non-homogeneous piezoelectric hollow cylinder, Int. J. Eng. Sci. 41 (2003) 1846–1868.
[7] T. Ikeda, Fundamentals of Piezoelectricity, Oxford University Press, Oxford, 1990.
[8] N. Kanbe, Y. Tomikawa, T. Takano, Powder-feeding device hollow cylindrical piezoelectric ceramics, Jpn. J. Appl. Phys. 32 (1993) 2405–2407.
[9] L.E. Kinsler, A.R. Frey, A.B. Coppens, J.V. Sanders, Fundamentals of Acoustics, fourth ed., Wiley, New York, 2000.
[10] J. Lighthill, Waves in Fluids, Cambridge University Press, Cambridge, 1978.
[11] R.V.N. Melnik, Numerical analysis of dynamic characteristics of coupled piezoelectric systems in acoustic media, Math. Comput. Simulat. 61 (2003) 497–507.
[12] J.L. Rose, Ultrasonic Waves in Solid Media, Cambridge University Press, Cambridge, 1999.
[13] M. Ruzzene, A. Baz, Active/passive control of sound radiation and power flow in fluid-loaded shells, Thin-Walled Struct. 38 (2000) 17–42.
[14] N.A. Shulga, S.I. Melnik, Energy analysis of axisymmetric wave propagation in a hollow liquid-containing piezoelectric cylinder, Int. Appl. Mech. 32 (1996) 81–88.
[15] S.A. Vera et al., Transverse vibrations of circular annular plates with edges elastically restrained against rotation, used in acoustic underwater transducers, Ocean Eng. 29 (2002) 1201–1208.
[16] M. Willatzen, Ultrasound transducer modeling—general theory and applications to ultrasound reciprocal systems, IEEE Trans. Ultrason. 48 (2001) 100–112.
[17] Z. Zhang, N. Vlahopoulos, S.T. Raveendra, Formulation of a numerical process for acoustic impedance sensitivity analysis based on the indirect BEM, Eng. Anal. BE 27 (2003) 671–681.
[18] D. Zhou et al., 3D vibration analysis of solid and hollow circular cylinders via Chebyshev–Ritz method, Comput. Methods Appl. Mech. Eng. 192 (2003) 1575–1589.
[19] O.C. Zienkiewicz, The Finite Element Method, McGraw-Hill, New York, 1977.